Applications of a MoM with High Order Impedance Boundary Condition for the Scattering Problem

Christian Daveau, Soumaya Oueslati, Svevo Bandelier

Applications of a MoM with High Order Impedance Boundary Condition for the Scattering Problem

Christian Daveau [*], Soumaya Oueslati [†], Svevo Bandelier [‡]

July 1, 2024

Abstract

In this paper, we study an integral equation method with high order impedance boundary condition (HOIBC) to solve Maxwell's equations in time harmonic regime. We present several numerical experiments.

1 Introduction

We are interested in solving the scattering problem using integral formulations with HOIBC [1], which leads to solving a variational problem in 3D and in 2D for a ground plane. In the first part, we study a PEC coated by a dielectric. Then we apply the moments method for a ground plane.

2 Integral formulation with HOIBC

The physical problem is described in Fig 1.

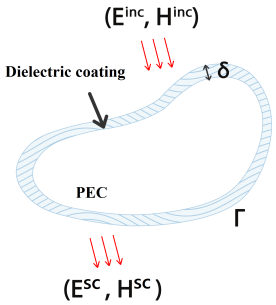

Figure 1: Scattering problem of dielectric coated conducting target

[*]CY Cergy Paris University, e-mail: christian.daveau@cyu.fr
[†]Nexio Toulouse France, e-mail: soumaya.oueslati1@nexiogroup.com
[‡]CY Cergy Paris University, e-mail: svevo.bandelier@cyu.fr

The dielectrically coated conducting objects fig. 1 can be modeled by an impedance boundary condition (IBC) at the surface, we are interested in higher-order impedance boundary conditions (HOIBC) (1), (see [1]), various methods are presented for computing the coefficients (a_0, a_j, b_j).

$$(I + b_1 L_D - b_2 L_R)\mathbf{E}_t = (a_0 I + a_1 L_D - a_2 L_R)(\mathbf{n} \times \mathbf{H}). \tag{1}$$

Thus leading to the following problem:

Problem 2.1. *Find* $(\boldsymbol{E}, \boldsymbol{H})$ *such as*

$$\begin{cases} \nabla \times \boldsymbol{E} + i\omega\mu \boldsymbol{H} = 0 \quad in \quad \Omega^e, \\ \nabla \times \boldsymbol{H} - i\omega\epsilon \boldsymbol{E} = 0 \quad in \quad \Omega^e, \\ (I + b_1 L_D - b_2 L_R)\boldsymbol{E}_t = (a_0 I + a_1 L_D - a_2 L_R)(\mathbf{n} \times \boldsymbol{H}) \quad in \ \ \Gamma, \\ \lim\limits_{r\to\infty} r(\boldsymbol{E} \times \boldsymbol{n}_r + \boldsymbol{H}) = 0. \end{cases} \tag{2}$$

We introduce the integral operators $(B - S)$ and $(P + Q)$ are defined as follows:

$$< (B - S)\phi, \boldsymbol{\psi} >= i \iint_\Gamma k\, G\, \phi \cdot \boldsymbol{\psi} - \frac{1}{k}\, G\, \nabla_y \cdot \phi\, \nabla_x \cdot \boldsymbol{\psi} \ \ dydx, \tag{3}$$

$$< (P + Q)\phi, \boldsymbol{\psi} >= \frac{1}{2} \int_\Gamma \boldsymbol{\psi} \cdot (\mathbf{n} \times \phi) \ \ dx + \iint_\Gamma (\boldsymbol{\psi} \times \phi) \cdot \nabla_x G \ \ dydx, \tag{4}$$

We then obtain the variational problem.

Problem 2.2. *Find* $U = (\mathbf{J}, \mathbf{M}) \in V = [H_{\mathrm{div}}(\Gamma) \cap H_{\mathrm{rot}}(\Gamma)]^2$ *such that:*

$$A(U, \Psi) =< I\mathbf{E}^{inc}, \boldsymbol{\Psi}_J > + < I\mathbf{H}^{inc}, \boldsymbol{\Psi}_M > \tag{5}$$

for all $\boldsymbol{\Psi} = (\boldsymbol{\Psi}_J, \boldsymbol{\Psi}_M) \in V$*, with the bilinear form* $A(U, \Psi)$ *is defined by :*

$$A(U, \Psi) =< Z_0(B - S)\boldsymbol{J}, \boldsymbol{\Psi}_J > + \frac{1}{Z_0} < (B - S)\boldsymbol{M}, \boldsymbol{\Psi}_M > + < Q\boldsymbol{M}, \boldsymbol{\Psi}_J > - < Q\boldsymbol{J}, \boldsymbol{\Psi}_M >$$

$$+ \frac{a_0}{2} < \boldsymbol{J}, \boldsymbol{\Psi}_J > + \frac{1}{2a_0} < \boldsymbol{M}, \boldsymbol{\Psi}_M > - \frac{a_1}{2} < \mathrm{div}_\Gamma \boldsymbol{J}, \mathrm{div}_\Gamma \boldsymbol{\Psi}_J > - \frac{b_2}{2a_0} < \mathrm{div}_\Gamma \boldsymbol{M}, \mathrm{div}_\Gamma \boldsymbol{\Psi}_M >$$

$$+ \frac{b_1}{2} < \mathrm{div}_\Gamma(\mathbf{n} \times \boldsymbol{M}), \mathrm{div}_\Gamma \boldsymbol{\Psi}_J > - \frac{b_2}{2} < \mathrm{div}_\Gamma \boldsymbol{M}, \mathrm{div}_\Gamma(\mathbf{n} \times \boldsymbol{\Psi}_J) > - \frac{b_1}{2a_0} < \mathrm{div}_\Gamma(\mathbf{n} \times \boldsymbol{M}), \mathrm{div}_\Gamma(\mathbf{n} \times \boldsymbol{\Psi}_M) >$$

$$+ \frac{a_1}{2a_0} < \mathrm{div}_\Gamma \boldsymbol{J}, \mathrm{div}_\Gamma(\mathbf{n} \times \boldsymbol{\Psi}_M) > - \frac{a_2}{2a_0} < \mathrm{div}_\Gamma(\mathbf{n} \times \boldsymbol{J}), \mathrm{div}_\Gamma \boldsymbol{\Psi}_M > - \frac{a_2}{2} < \mathrm{div}_\Gamma(\mathbf{n} \times \boldsymbol{J}), \mathrm{div}_\Gamma(\mathbf{n} \times \boldsymbol{\Psi}_J) >$$

In the next section, we are going to give an alternative proof that Problem 2.2 is well-posed by analysing the bilinear form A defined on $V = [H_{\mathrm{div}}(\Gamma) \cap H_{\mathrm{rot}}(\Gamma)]^2$.

We have the following result.

Theorem 2.1. *The variational problem* 2.2 *admits a unique solution if the coefficients satisfy*

the following conditions:

$$\begin{cases} \Re(a_0) > 0, \\ \Re(a_1) < -\frac{|q_1|}{2}, \\ \Re(b_1 a_0^*) < -\frac{|q_1|}{2} \\ \Re(a_2) < -\frac{|q_2|}{2} \\ \Re(b_2 a_0^*) < -\frac{|q_2|}{2} \end{cases} \tag{6}$$

where : $q_1 = b_1|a_0| + a_1^* a_0/|a_0|$ *et* $q_2 = b_2|a_0| + a_2^* a_0/|a_0|$.

3 Discretization and operators' approximation

The obtained variational Problem 5 is solved with the method of moments (MoM) [2] using Galerkin testing procedure, which requires discretizing the contour defining the surface Γ into triangles T.

$$\Gamma_h = \bigcup_{n=1}^{N_T} T_n.$$

To discretize the variational problem, we employ a non-conformal approach, the Galerkin method is employed utilizing RAO-Wilton-Glisson RWG basis functions defined on the space $W = H_{\text{div}}^{-1/2}$, i,e. , the equivalent currents on the surface J and M are approximated on a set of N_e basis functions using RWG functions $f_i(x)$ with the unknown are the flows such as:

$$\mathbf{J}(x) = \sum_{i=1}^{Ne} J_i \mathbf{f}_i(x), \quad \mathbf{M}(x) = \sum_{i=1}^{Ne} M_i \mathbf{f}_i(x). \tag{7}$$

On each triangle, the current is written as a linear combination of 3 functions of base associated with 3 edges of a triangle. If n is a common edge of two triangles then:

$$\mathbf{f}_n(x) = \begin{cases} \frac{l_n}{2|T_n^+|}(x - a_{i-1}^+) & if\ x \in T_n^+ \\ \frac{l_n}{2|T_n^-|}(a_{j-1}^- - x) & if\ x \in T_n^- \\ 0 & if\ x \notin T_n^+ \cup T_n^- \end{cases} \tag{8}$$

we define also its divergence:

$$\nabla_\Gamma \cdot \mathbf{f}_n(x) = \begin{cases} +\frac{l_n}{|T_n^+|} & if\ x \in T_n^+ \\ -\frac{l_n}{|T_n^-|} & if\ x \in T_n^- \\ 0 & if\ x \notin T_n^+ \cup T_n^-. \end{cases} \tag{9}$$

By arbitrary definition, the current flows from the first triangle of the zone T_n^+ to the second triangle of the zone T_n^-. a_{i-1}^+ and a_{j-1}^- are the opposite vertices of the edge n in T_n^+ and T_n^- respectively. $|T_n^\pm|$ designates the area of the triangle $T_n^\pm$ and the length of the common edge is l_n. Through the use of the decomposition of surface electric and magnetic densities (7), we inject them into the variational problem (2.2).

This procedure converts the coupled set of integral equations into a matrix which may be cast into the form.

$$A^h(U_h, \Psi_h) = \sum_{i=1}^{Ne} < \mathbf{E}^{inc}, \mathbf{f}_i > + \sum_{i=1}^{Ne} < \mathbf{H}^{inc}, \mathbf{f}_i > \tag{10}$$

where

$$A^h(U_h, \Psi_h) = \sum_{i,j=1}^{N_e} < Z_r Z_0 \ (B-S)\mathbf{f}_j, \mathbf{f}_i > J_j + Z_r^{-1} Z_0^{-1} \sum_{i,j=1}^{N_e} < (B-S)\mathbf{f}_j, \mathbf{f}_i > M_j$$

$$+ \sum_{i,j=1}^{N_e} < Q\mathbf{f}_j, \mathbf{f}_i > M_j - \sum_{i,j=1}^{N_e} < Q\mathbf{f}_j, \mathbf{f}_i > J_j + \frac{a_0}{2} \sum_{i,j=1}^{N_e} < \mathbf{f}_j, \mathbf{f}_i > J_j + \frac{1}{2a_0} \sum_{i,j=1}^{N_e} < \mathbf{n}\times\mathbf{f}_j, \mathbf{n}\times\mathbf{f}_i > M_j$$

$$+ \frac{a_1}{2} \sum_{i,j=1}^{N_e} < \nabla_\Gamma \nabla_\Gamma \cdot \mathbf{f}_j, \mathbf{f}_i > J_j - \frac{a_2}{2} \sum_{i,j=1}^{N_e} < \nabla_\Gamma \nabla_\Gamma \cdot (\mathbf{n} \times \mathbf{f}_j), \mathbf{n} \times \mathbf{f}_i > J_j$$

$$- \frac{b_1}{2} \sum_{i,j=1}^{N_e} < \nabla_\Gamma \nabla_\Gamma \cdot \mathbf{f}_j, \mathbf{n} \times \mathbf{f}_i > M_j + \frac{b_2}{2} \sum_{i,j=1}^{N_e} < \nabla_\Gamma \nabla_\Gamma \cdot (\mathbf{n} \times \mathbf{f}_j), \mathbf{f}_i > M_j$$

$$+ \frac{b_1}{2a_0} \sum_{i,j=1}^{N_e} < \nabla_\Gamma \nabla_\Gamma \cdot (\mathbf{n} \times \mathbf{f}_j), \mathbf{n} \times \mathbf{f}_i > M_j - \frac{b_2}{2a_0} \sum_{i,j=1}^{N_e} < \nabla_\Gamma \nabla_\Gamma \cdot \mathbf{f}_j, \mathbf{f}_i > M_j$$

$$- \frac{a_1}{2a_0} \sum_{i,j=1}^{N_e} < \nabla_\Gamma \nabla_\Gamma \cdot (\mathbf{n} \times \mathbf{f}_j), \mathbf{f}_i > J_j + \frac{a_2}{2a_0} \sum_{i,j=1}^{N_e} < \nabla_\Gamma \nabla_\Gamma \cdot \mathbf{f}_j, \mathbf{n} \times \mathbf{f}_i > J_j;$$

We seek an approximate solution to the discrete problem (10). To solve it, we first give notations for the integral operators arising from the Higher-Order Integral Boundary Conditions (HOIBC) involved in the discrete problem, defined as follows:

$$L_{ij} = \int_{\Gamma_h} \mathbf{f}_i \cdot \mathbf{f}_j ds, \tag{11}$$

$$D_{ij} = \int_{\Gamma_h} \nabla_\Gamma \nabla_\Gamma \cdot \mathbf{f}_j \cdot \mathbf{f}_i ds \tag{12}$$

$$E_{ij} = \int_{\Gamma_h} \nabla_\Gamma \nabla_\Gamma \cdot \mathbf{f}_j \cdot \mathbf{n} \times \mathbf{f}_i ds, \tag{13}$$

$$G_{ij} = \int_{\Gamma_h} \nabla_\Gamma \nabla_\Gamma \cdot (\mathbf{n} \times \mathbf{f}_j) \cdot \mathbf{n} \times \mathbf{f}_i ds. \tag{14}$$

We study discretzations for these operators.

3.1 The jump formula

Definition 3.1. *Formula for the jump across a bounded surface*

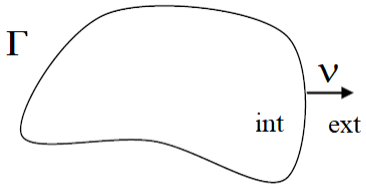

Let Ω be an open set of $\mathbb{R}^3$, with a Lipschitz boundary Γ, F a regular function in $\mathbb{R}^3$, such that C^1-regular on either side of Γ. Then the jump of the discontinuous function F through Γ is denoted by:

$$[F]_\Gamma = F^{int} - F^{ext}$$

with F^{int}, F^{ext} are the values of F inside and outside the domain bounded by Γ respectively. The normal $\boldsymbol{\nu}$ to Γ is oriented inside out.

This definition leads to the formulas of the gradient and the divergence in the sense of distribution for functions which are discontinuous at this interface:

Proposition 3.2. *With the regularity hypotheses of the function F, we have:*
The gradient and the divergence in the sense of the distributions defined for functions which are discontinuous at an interface Γ are given by:

$$\nabla F = (\nabla F) - S_\Gamma([F]\boldsymbol{\nu}) \tag{15}$$

$$\nabla \cdot F = (\nabla \cdot F) - S_\Gamma([F \cdot \boldsymbol{\nu}]) \tag{16}$$

where (∇F) and $(\nabla \cdot F)$ are respectively the usual gradient and divergence of the function where they exist and S_Γ is the operator defined by:

$$< S_\Gamma(F), \varphi >= \int_\Gamma F(x)\varphi(x)\, dx.$$

One observes the presence of discontinuity through the edges which deteriorates the conditioning of the operators, an approximation method is thus necessary.
According to (15) the gradient of piecewise constant functions F is written in this form:

$$< \nabla_\Gamma F, \varphi >= -[F]_{/\Gamma} \int_\Gamma \boldsymbol{\nu}(x) \cdot \varphi(x)\, dx\ ,\ \ \forall \varphi \in D(\mathbb{R}^3)^3 \tag{17}$$

one has upon the application of $F = \nabla_\Gamma \cdot \mathbf{f}$ in (17), so that $< \nabla_\Gamma \nabla_\Gamma \cdot f, \varphi >$ can be written as

$$< \nabla_\Gamma \nabla_\Gamma \cdot \mathbf{f}, \varphi >= -[\nabla_\Gamma \cdot \mathbf{f}]_{/\Gamma} \int_\Gamma \boldsymbol{\nu}(x) \cdot \varphi(x)\, dx\ , \quad \forall \varphi \in D(\mathbb{R}^3)^3 \tag{18}$$

3.2 Integral operators' approximation

To have an explicit expression of the operators, we first define the jump of a piecewise constant function f with respect to an edge i [3].

Definition 3.3. *The jump of a piecewise constant function f with respect to an edge i:*

$$\begin{aligned} [\mathbf{f}]_{/i} &= (\varepsilon_i f)^{T_i^+} + (\varepsilon_i f)^{T_i^-} \\ &= \varepsilon_i^{T_i^+} f^{T_i^+} + \varepsilon_i^{T_i^-} f^{T_i^-} \\ &= f^{T_i^+} - f^{T_i^-} \end{aligned}$$

with the trace of f on T_i^+ and T_i^- denoted by $f^{T_i^+}$ and $f^{T_i^-}$ respectively.
The function ε_i is defined by:

$$\varepsilon_i(x) = \begin{cases} 1 \quad on \quad T_i^+, \\ -1 \ on \quad T_i^-, \\ 0 \quad otherwise. \end{cases}$$

3.2.1 Approximation of operator D

We will explain the method of calculating the elements of matrices D_{ij}. By applying the differential operators property (18) to the D operator [3]:

$$\begin{aligned} D_{ij} &= \int_{\Gamma_h} \nabla_\Gamma \nabla_\Gamma \cdot \mathbf{f}_j \cdot \mathbf{f}_i\, dS \\ &= -l_i [\nabla \cdot \mathbf{f}_j]_{/l} \int_l \boldsymbol{\nu}_l \cdot \mathbf{f}_i\, ds \end{aligned}$$

with $\boldsymbol{\nu}_l^+$ (respectively $\boldsymbol{\nu}_l^-$) is the outgoing normal to edge l which goes from T_l^+ to T_l^- (respectively from T_l^- to T_l^+) in the plane of the triangle.
We deduce the expression of the operator D_{ij}:

$$D_{ij} = -\, l_i [\nabla \cdot \mathbf{f}_j]_{/i}. \tag{19}$$

Using definition 3.1, the divergence jump of RWG functions (8):

$$\begin{aligned}
\left[\nabla\cdot\mathbf{f}_j\right]_{/i} &= \left[(\varepsilon_i\nabla\cdot\mathbf{f}_j)^{T_i^+} + (\varepsilon_i\nabla.\mathbf{f}_j)^{T_i^-}\right] &(20)\\
&= {\varepsilon_i}^{T_i^+}\nabla\cdot{\mathbf{f}_j}^{T_i^+} + {\varepsilon_i}^{T_i^-}\nabla\cdot{\mathbf{f}_j}^{T_i^-} &(21)\\
&= {\varepsilon_i}^{T_i^+}{\varepsilon_j}^{T_i^+}\frac{l_j}{|T_j|^{T_i^+}} + {\varepsilon_i}^{T_i^-}{\varepsilon_j}^{T_i^-}\frac{l_j}{|T_j|^{T_i^-}} &(22)
\end{aligned}$$

so the D_{ij} (19) can therefore be written as

$$D_{ij} = -l_i\left({\varepsilon_i}^{T_i^+}{\varepsilon_j}^{T_i^+}\frac{l_j}{|T_j|^{T_i^+}} + {\varepsilon_i}^{T_i^-}{\varepsilon_j}^{T_i^-}\frac{l_j}{|T_j|^{T_i^-}}\right).$$

3.2.2 Approximation of operator E

Similarly as for the operator D, using the definition of the gradient of piecewise constant function, the operator E can be written as :

$$\begin{aligned}
E_{ij} &= \int_{\Gamma_h}\nabla_\Gamma\nabla_\Gamma\cdot\mathbf{f}_j\cdot\mathbf{n}\times\mathbf{f}_i\,ds\\
&= -\sum_{l=1}^{Ne}\left[\nabla\cdot\mathbf{f}_j\right]_{/l}\int_l\ \boldsymbol{\nu}_l\cdot\mathbf{n}\times\mathbf{f}_i\,ds
\end{aligned}$$

We make an approximation of $\int_l\ \boldsymbol{\nu}_l\cdot\mathbf{n}\times\mathbf{f}_i\,ds$ to translate the discontinuity of the normals which is:

$$\int_l\boldsymbol{\nu}_l\cdot\mathbf{n}\times\mathbf{f}_i\,ds = \frac{1}{2}\left(\int_l\boldsymbol{\nu}_l\cdot\mathbf{n}\times\mathbf{f}_i\,ds\right)_{T_i^+} + \frac{1}{2}\left(\int_l\boldsymbol{\nu}_l\cdot\mathbf{n}\times\mathbf{f}_i\,ds\right)_{T_i^-} \quad (23)$$

To determine this integral, it is necessary to distinguish several geometric configurations.

$$\int_l\boldsymbol{\nu}_l\cdot\mathbf{n}\times\mathbf{f}_i\,ds = \begin{cases}
\frac{1}{2}(\int_l\ \boldsymbol{\nu}_l^+\cdot\mathbf{n}_{T_i^+}\times\mathbf{f}_i^+\,ds + \int_l\ \boldsymbol{\nu}_l^-\cdot\mathbf{n}_{T_i^-}\times\mathbf{f}_i^-\ ,ds), & \text{if } i=l\\
\frac{1}{2}\int_l\ \boldsymbol{\nu}_l^+\cdot\mathbf{n}_{T_l^+}\times\mathbf{f}_i^\pm\,ds, & \text{if } i\in T_l^+\\
\frac{1}{2}\int_l\ \boldsymbol{\nu}_l^-\cdot\mathbf{n}_{T_l^-}\times\mathbf{f}_i^\pm\,ds, & \text{if } i\in T_l^-
\end{cases}$$

The expression of the operator E is then written:

$$\begin{aligned}
E_{ij} &= -\frac{1}{2}([\nabla.\mathbf{f}_j]_{/i}\left(\int_{l=i}\boldsymbol{\nu}_i^+\cdot\mathbf{n}_{\mathbf{T_i^+}}\times\mathbf{f}_i^+\,ds + \int_{l=i}\boldsymbol{\nu}_i^-\cdot\mathbf{n}_{T_i^-}\times\mathbf{f}_i^-\,ds\right)\\
&+ \sum_{l\in T_i^+=T_l^+}[\nabla.\mathbf{f}_j]_{/l}\int_l\boldsymbol{\nu}_l^+\cdot\mathbf{n}_{T_l^+}\times\mathbf{f}_i^+\,ds + \sum_{l\in T_i^+=T_l^-}[\nabla.\mathbf{f}_j]_{/l}\int_l\boldsymbol{\nu}_l^-\cdot\mathbf{n}_{\mathbf{T_l^-}}\times\mathbf{f}_i^+\,ds\\
&+ \sum_{l\in T_i^-=T_l^+}[\nabla.\mathbf{f}_j]_{/l}\int_l\boldsymbol{\nu}_l^+\cdot\mathbf{n}_{T_l^+}\times\mathbf{f}_i^-\,ds + \sum_{l\in T_i^-=T_l^-}[\nabla.\mathbf{f}_j]_{/l}\int_l\boldsymbol{\nu}_l^-\cdot\mathbf{n}_{T_l^-}\times\mathbf{f}_i^-\ ,ds).
\end{aligned}$$

The integral operator which is defined by:

$$\int_{\Gamma_h} L_D(\mathbf{n}\times\mathbf{f}_j)\cdot\mathbf{f}_i\,ds$$

is the adjoint operator of operator E_{ij}.

3.2.3 Approximation of the G operator

Employing the definition of the operator G and the jump formula, we deduce the result for the operator E using similar procedure, we find [4]:

$$\begin{aligned}
G_{ij} &= \int_{\Gamma_h} \nabla_\Gamma\nabla_\Gamma\cdot(\mathbf{n}\times\mathbf{f}_j)\cdot(\mathbf{n}\times\mathbf{f}_i)\,ds \\
&= -\frac{1}{2}([\nabla.(\mathbf{n}\times\mathbf{f}_j)]_{/i}\left(\int_{l=i}\boldsymbol{\nu}_i^+\cdot\mathbf{n}_{\mathbf{T_i^+}}\times\mathbf{f}_i^+\,ds+\int_{l=i}\boldsymbol{\nu}_i^-\cdot\mathbf{n}_{T_i^-}\times\mathbf{f}_i^-\,ds\right) \\
&+ \sum_{l\in T_i^+=T_l^+}[\nabla.(\mathbf{n}\times\mathbf{f}_j)]_{/l}\int_l\boldsymbol{\nu}_l^+\cdot\mathbf{n}_{T_l^+}\times\mathbf{f}_i^+\,ds+\sum_{l\in T_i^+=T_l^-}[\nabla.(\mathbf{n}\times\mathbf{f}_j)]_{/l}\int_l\boldsymbol{\nu}_l^-\cdot\mathbf{n}_{\mathbf{T_l^-}}\times\mathbf{f}_i^+\,ds \\
&+ \sum_{l\in T_i^-=T_l^+}[\nabla.(\mathbf{n}\times\mathbf{f}_j)]_{/l}\int_l\boldsymbol{\nu}_l^+\cdot\mathbf{n}_{T_l^+}\times\mathbf{f}_i^-\,ds+\sum_{l\in T_i^-=T_l^-}[\nabla.(\mathbf{n}\times\mathbf{f}_j)]_{/l}\int_l\boldsymbol{\nu}_l^-\cdot\mathbf{n}_{T_l^-}\times\mathbf{f}_i^-\,ds).
\end{aligned}$$

The jump calculation $[\nabla\cdot(\mathbf{n}\times\mathbf{f}_j)]_{/l}$ is based on the calculation of the adjoint operator of E.

4 Numerical experiments

In this section, several examples will be presented to show the accuracy of the proposed method and correctness of the developed formulation after implementing it into MoM code ([4],[5]). A standard spherical coordinate system is used for the body of revolution model with the z axis being the axis of revolution. Several geometries and different types of dielectric material (electric permittivity ϵ_r and magnetic permeability μ_r) are also presented. The first example is considered for validating the accuracy of the code developed while the remaining examples are regarded to produce some new results which cannot be found elsewhere in literature.

First, we consider a coated conductive sphere having a radius of $r_2 = 1.8\lambda$, thickness of coating layer is $0.05m$ (fig. 2) with a relative permittivity of $\epsilon_r = 5$ and a relative permeability of $\mu_r = 1$. The exact series-solution of this geometry is available and is used here to validate the results of the proposed formulation. The bistatic RCS for the $\theta\theta$-polarization at $0.45GHz$ are computed and the results obtained (fig. 3) are compared with Mie series solutions. Figure 3 illustrates three results, Mie's analytical result and different mesh densities using the new approximation method. Good agreements have been observed in the comparisons.

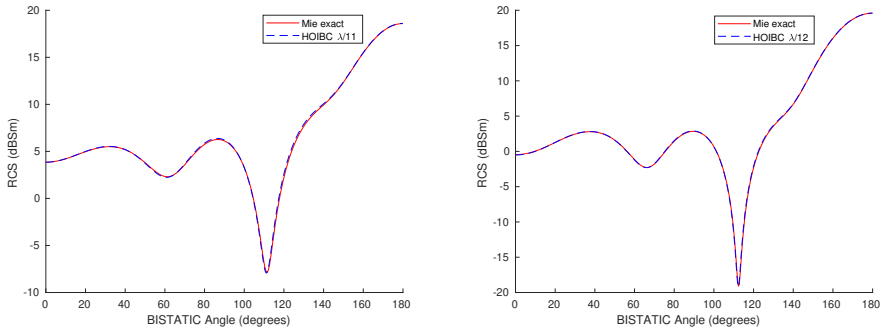

(a) $\epsilon_r = 1 - i$ and $\mu_r = 1$ (b) $\epsilon_r = 2 - 3i$ and $\mu_r = 1 - i$

Figure 4: $\theta\theta$ component of the bistatic RCS for a coated conductive sphere with frequency $f = 0.190986GHz$, layer thickness $\delta \simeq 0.05\lambda$. Exact Mie solution and HOIBC solution

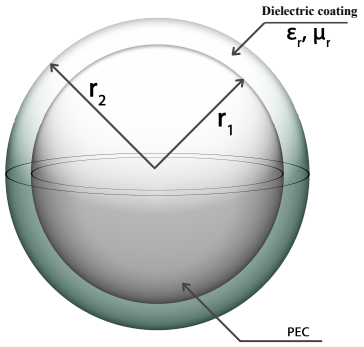

Figure 2: geometry of a coated conductive sphere

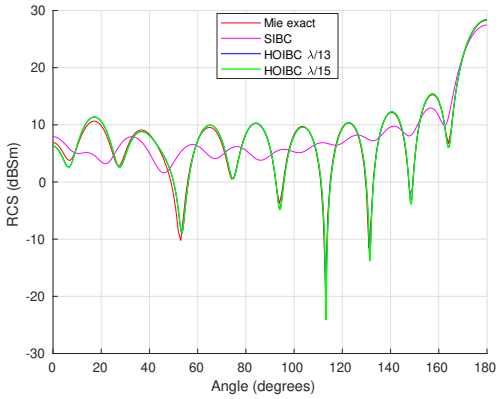

Figure 3: $\theta\theta$ component of the bistatic RCS for a coated conductive sphere with frequency $f = 0.45GHz$, layer thickness $\delta = 0.09\lambda$. Exact Mie solution and HOIBC solutions.

Now, we will choose a complex configurations of permittivity and permeability. In fig. 4a and fig. 4b, when we substitute the complex values for permeability and permittivity, we ob-

serve a very good agreement between the analytical solution of Mie and the numerical results obtained using the HOIBC method. In our study, we compared our method to the Lagrange multiplier method proposed in [1]. Since the analytical solution is available for comparison, we computed the error for different meshes using the infinity norm for both methods. Additionally, we measured the CPU time (in seconds) for system resolution and the total memory occupation of the matrix (in Go). We begin by considering the case where $\epsilon_r = 5$ and $\mu_r = 1$.

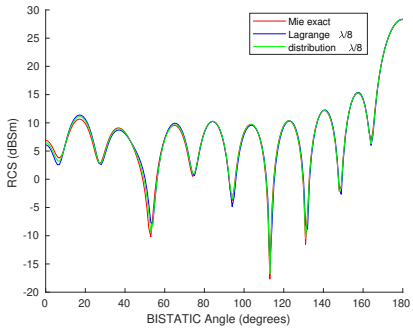

(a) Comparison between Lagrange solution and distribution solution of the corresponding mesh $\lambda/8$. The Mie series solution is used as reference data.

number of unknowns	mesh density	Distribution			Lagrange		
		$\|.\|_\infty$	CPU(s)	Mem(Go)	$\|.\|_\infty$	CPU(s)	Mem(Go)
55788	$\lambda/8$	0.018	343.66	27.2	0.032	385.7	27.2
101760	$\lambda/10$	0.018	1287.16	84.81	0.032	1365.9	84.81
125376	$\lambda/11$	0.0152	2326.97	118.37	0.032	2602.63	118.37
186684	$\lambda/14$	0.0104	4529.9	285.16	0.031	4736.36	285.16

(b) Comparison in terms of relative error and memory usage with respect to mesh density

Figure 5: Values of error computed using two approximations of integral operators with the different mesh with $\epsilon_r = 5$ and $\mu_r = 1$.

In fig. 5a, it is evident that the results of both methods compare well with the exact solution. But, from the above discussion in fig. 5b, we can see that the other method suffers a drastic increase in the computation cost as the number of unknowns increases. The matrix size, and hence, both the filling and solving times grow substantially. On the other hand, our method has a better performance regarding the CPU times where the computation cost is substantially lower. In the light of these factors, our method is more appealing than the other formulation for simulating large-scale problems where the reduction of CPU times becomes an essential and crucial issue. Now we compute the error with complex permitivity and permeability $\epsilon_r = 2 - 3i$

and $\mu_r = 1 - i$.

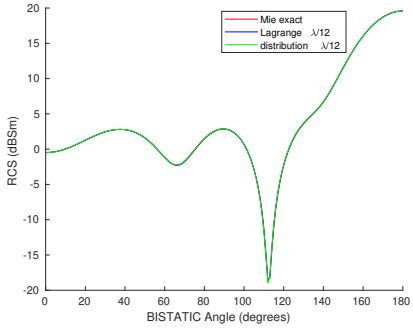

(a) Comparison between Lagrange solution and distribution solution for the mesh $\lambda/12$.

number of unknowns	mesh density	Distribution			Lagrange		
		$\|.\|_\infty$	CPU(s)	Mem(Go)	$\|.\|_\infty$	CPU(s)	Mem(Go)
4956	$\lambda/8$	0.013	1.9	0.32	0.0122	1.95	0.32
10824	$\lambda/12$	0.0051	11.69	1.32	0.0039	12.75	1.32
44664	$\lambda/25$	0.005	54.28	19.26	0.0026	76.05	19.26

(b) Comparison in terms of error and memory usage with respect to mesh density

Figure 6: Values of relative error computed using two approximations of integral operators with the different mesh with $\epsilon_r = 2 - 3i$ and $\mu_r = 1 - i$.

According to the tests presented above, it can be concluded that Lagrange approximation has a good accuracy independently with respect to the number of unknowns, while our approximation has the best performance in terms of computational cost.

We will now transition to a different geometry where no analytical scattering solution is available as a reference. To obtain the reference results, we compare our method to the reference PMCHWT formulation ([6],[7],[8]). We move on to the case of an ellipsoid is with dielectric parameters as depicted in fig. 7a, we choose a coating thickness $\delta = 0.1\lambda$.

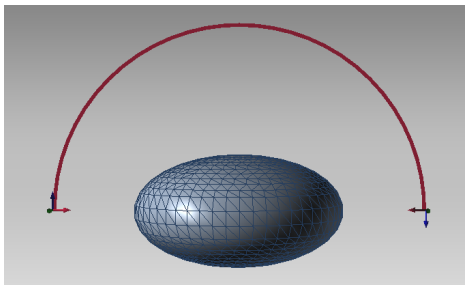

(a) Surfacic mesh of the ellipsoid. $\epsilon_r = 5$ and $\mu_r = 1$.

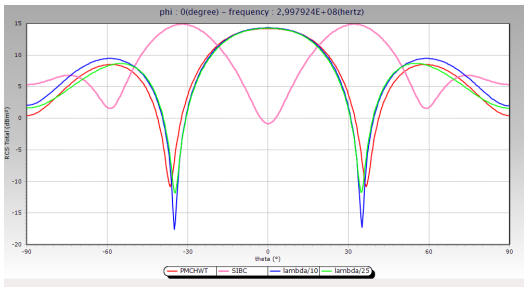

(b) $\theta\theta$ component of the monostatic RCS with frequncy $f = 0.3GHz$. Reference PMCHWT and HOIBC solutions.

Figure 7a presents surface mesh of ellipsoid geometry and fig. 7b plots $\theta\theta$ component of the monostatic RCS with the solution using SIBC and two mesh densities $\lambda/10$ and $\lambda/25$ and we compare it to PMCHWT reference. We notice that we obtain a good accuracy compared with the reference PMCHWT when we use a finer mesh.

In the sequel, sharp-edged targets will be simulated by the suggested method to verify the stability of the proposed formulation. We consider the case of coated PEC almond. Its total length is $4.169\lambda_0$, where λ_0 is the vacuum wavelength, and the dielectric parameters are $\epsilon_r = 4$ and $\mu_r = 1$. A 0.5-GHz monostatic RCS, $\theta\theta$-polarized incident wave is incident from the tip of the almond. Figure 8a shows the mesh configuration of this problem fig. 8b.

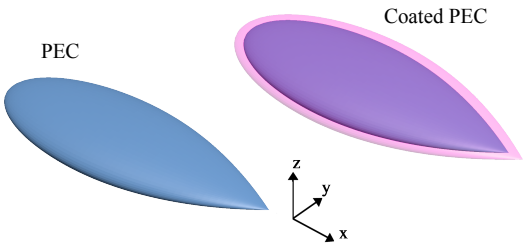

(a) Problem description

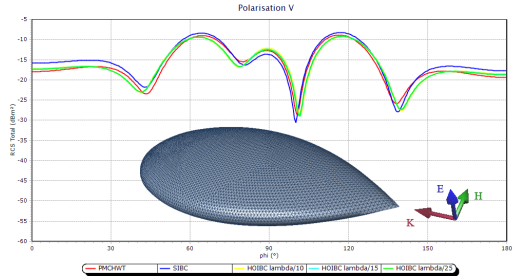

(b) Surface mesh for nasa almond geometry. Plot of SIBC , HOIBC with different mesh density and PMCHWT reference

Figure 8: Scattering analysis for the NASA almond with $\epsilon_r = 4$ and $\mu_r = 1$. A 0.5-GHz monostatic RCS, $\theta\theta$-polarized incident wave is incident from the tip of the almond

Figure 8b plots different HOIBC mesh densities solutions and SIBC solution. It is clear that HOIBC converge to PMCHWT reference and more accurate compared to SIBC.

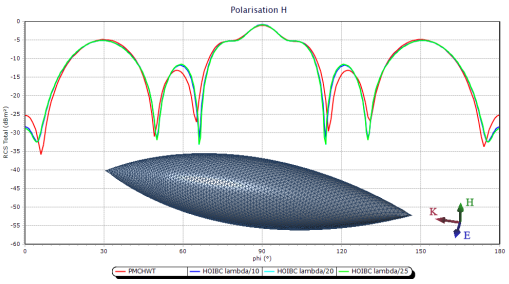

(a) Surface mesh for simple-ogival geometry. Plot HOIBC with different mesh density and PMCHWT reference

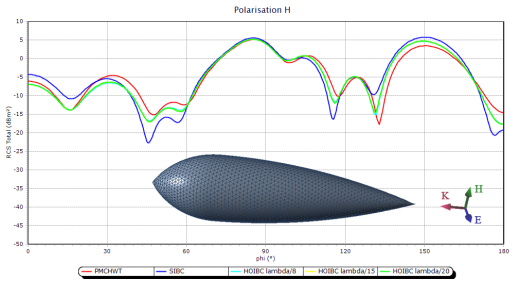

(b) Surface mesh for double-ogival geometry. Plot of SIBC , HOIBC with different mesh density and PMCHWT reference

Figure 9: Scattering analysis for different types of ogives (double fig. 9a and simple fig. 9b). A monostatic RCS, $\phi\phi$-polarized incident wave is incident from the tip of the ogives

Based on the tests on the sphere (see fig. 2), ellipsoid (see fig. 7a), and double-ogive (see fig. 9b), it can be concluded that the Higher Order Impedance Boundary Condition (HOIBC) approximation exhibits good accuracy. However, the Standard Impedance Boundary Condition (SIBC) approximation demonstrates poor accuracy in both simple and complex cases.

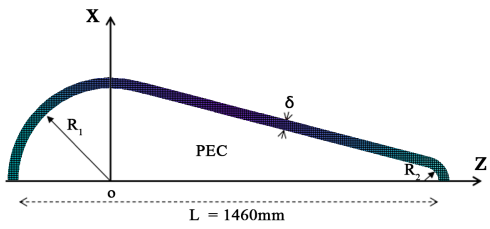

(a) Geometry of coated conductive sphere-cone-sphere.$R_1 = 315mm, R2 = 50mm$.
$\delta = 0.02m$, $\epsilon_r = 5$ and $\mu_r = 1$.

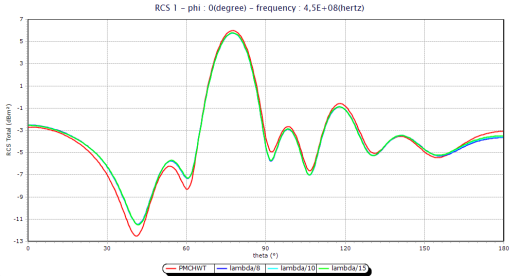

(b) $\phi\phi$ component of the monostatic RCS with frequency $f = 0.45GHz$. Reference PMCHWT and HOIBC solutions.

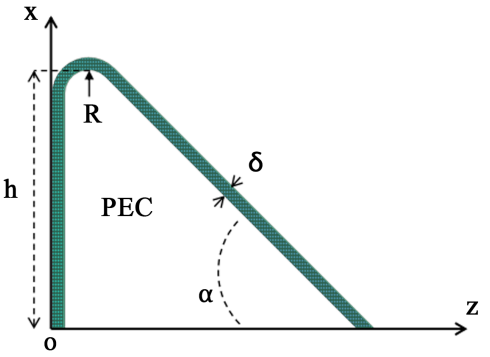

(c) Geometry of cone. $h = 716mm$, $R = 66mm$, $\alpha = 45°$ and $\delta = 0.034m$, $\epsilon_r = 2 - i$ and $\mu_r = 1$.

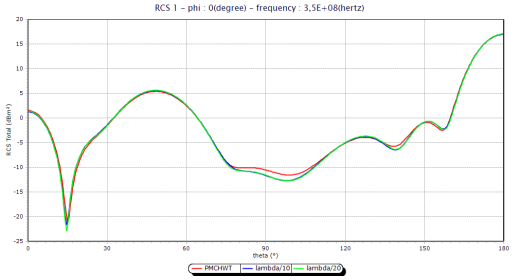

(d) $\phi\phi$ component of the monostatic RCS with frequency $f = 0.35GHz$. Reference PMCHWT and HOIBC solutions.

Figure 10: Performance comparison of different mesh of HOIBC formulation with respect to PMCHWT reference of conic geometries

Figure 10a and fig. 10c presents geometrical parameters of coated conductive sphere-cone-sphere and coated conductive cone respectively. Figure 10b and fig. 10d plots $\phi\phi$ component of the monostatic RCS with different mesh densities and frequencies compared with PMCHWT reference. We observe that, in both geometries,increasing the number of unknowns yields good accuracy regardless of the frequency. As shown in fig. 10d, the two curves of HOIBC solutions agree excellently with each other comparing to the reference.

We choose now another conic geometry (fig. 11) that is coated with a complex homogeneous material layer $\epsilon_r = 1 - i$ and $\mu_r = 1$.

Figure 11a shows the mesh configuration of cone and fig. 11b display the results obtained. We can observe that as the mesh density increases, the HOIBC solutions exhibit a strong agreement with the reference PMCHWT. This can be attributed to the excellent performance of the HOIBC operators employed in the formulation.

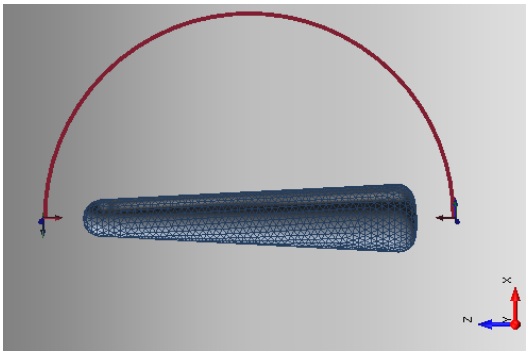

(a) Monostatic RCS of a $1.312m \times 1.312m \times 0.798m$ of a coated PEC cone body ($\delta = 0.05m$, $\epsilon_r = 1 - i$ and $\mu_r = 1$) at $0.19GHz$.

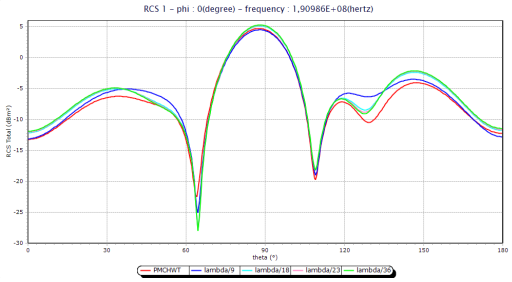

(b) $\theta\theta$ RCS component. Reference PMCHWT and HOIBC solutions.

Figure 11: Performance comparison of different mesh of HOIBC formulation with respect to PMCHWT reference

We gave some preliminary results indicating good accuracy behavior of our method compared to the popular PMCHWT equation. Numerical examples demonstrate that the developed new formulation lead to clear improvements in the convergence rates.

5 Variationnal formulation with HOIBC for a ground plane

We described the problem see Fig. 12. Here, we consider TM polarization and apply image

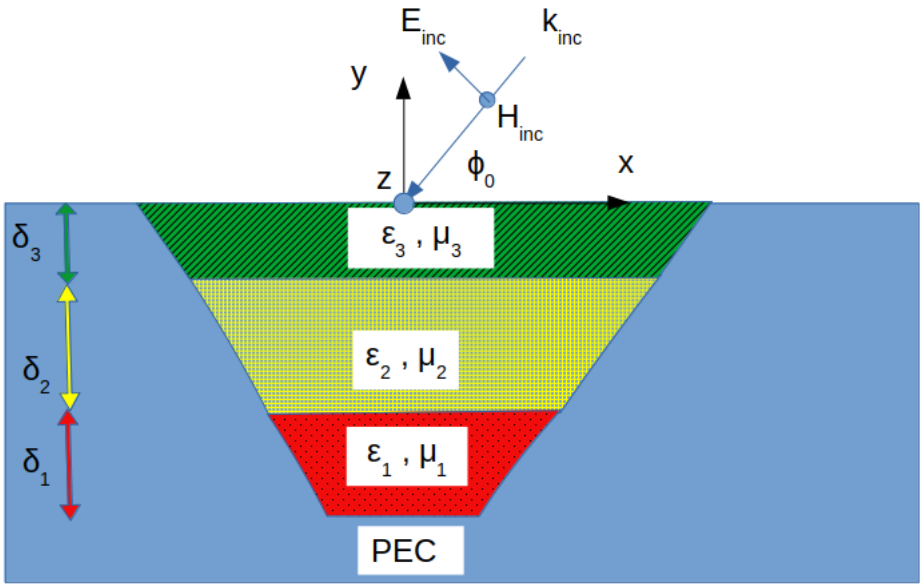

Figure 12: Ground plane

theory and principe of equivalence. Then, we propose the following variational formulation:

$$
\begin{aligned}
&\int_{x_l}^{x_r} M_z(x)\varphi(x)\ dx \\
&+ \frac{\omega\epsilon_0}{2}\int_{x_l}^{x_r}\int_{x_l}^{x_r} a_0(x)\ H_0^{(2)}(k_0|x-x'|)M_z(x')\varphi(x)dx'dx \\
&+ \frac{\omega\epsilon_0}{2}\int_{x_l}^{x_r}\int_{x_l}^{x_r} a_1(x)\ (\partial_x^2 H_0^{(2)}(k_0|x-x'|))M_z(x')\varphi(x)dx'dx \\
&+ \int_{x_l}^{x_r} b_1(x)\partial_x^2 M_z(x)\varphi(x)dx \\
&= 2\int_{x_l}^{x_r}(a_0(x) - a_1(x)k_0^2\cos(\phi_0)^2)e^{jk_0\cos(\phi_0)x}\varphi(x)dx
\end{aligned}
\tag{24}
$$

6 Meixner's conditions

We have to apply HOIBC in an interior domain since singularity appears at the ends of the domain. We then apply Meixner's conditions to take account the discontinuity PEC/dielectric material.

$$
\frac{M_1}{(\frac{\Delta}{2})^{t_l-1}} = \frac{M_2}{(\frac{3\Delta}{2})^{t_l-1}} \tag{25}
$$

$$
\frac{M_N}{(\frac{\Delta}{2})^{t_r-1}} = \frac{M_{N-1}}{(\frac{3\Delta}{2})^{t_r-1}} \tag{26}
$$

To calculate t, we etablish an equation in t, with Φ_1 and Φ_2 given by Figure 13 :

$$\frac{\tan(t\Phi_1)}{\epsilon_1} + \frac{\tan(t\Phi_2)}{\epsilon_2} = 0 \tag{27}$$

Theses conditions are based on a equivalence relation on the normal electric field :

$$E_\rho \sim \rho^{t-1} \tag{28}$$

, with ρ the distance to the edge.

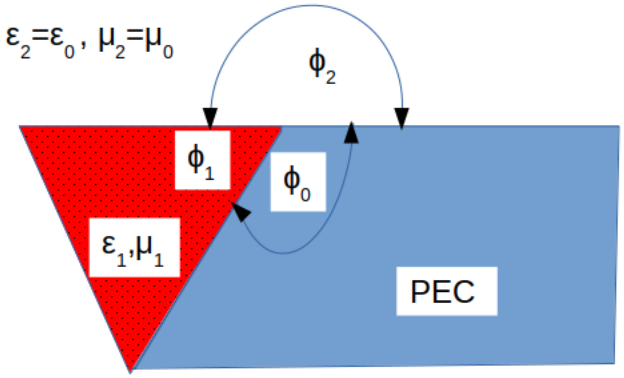

Figure 13: Calculation of t

7 Numerical results

With 45 points, our HOIBC+edges almost coincides with the FEM. So we hypothesize that the size of a segment (3/45 m) constitutes a good balance between the edge zone and the HOIBC zone . By calculation we find that the length of a segment is approximately equal to $\frac{\lambda}{6.70}$, for the frequency and the properties of the material in our example. We specify that λ corresponds to the wavelength in the dielet. Note that for each ϵ_r it is necessary to calculate a new t0.

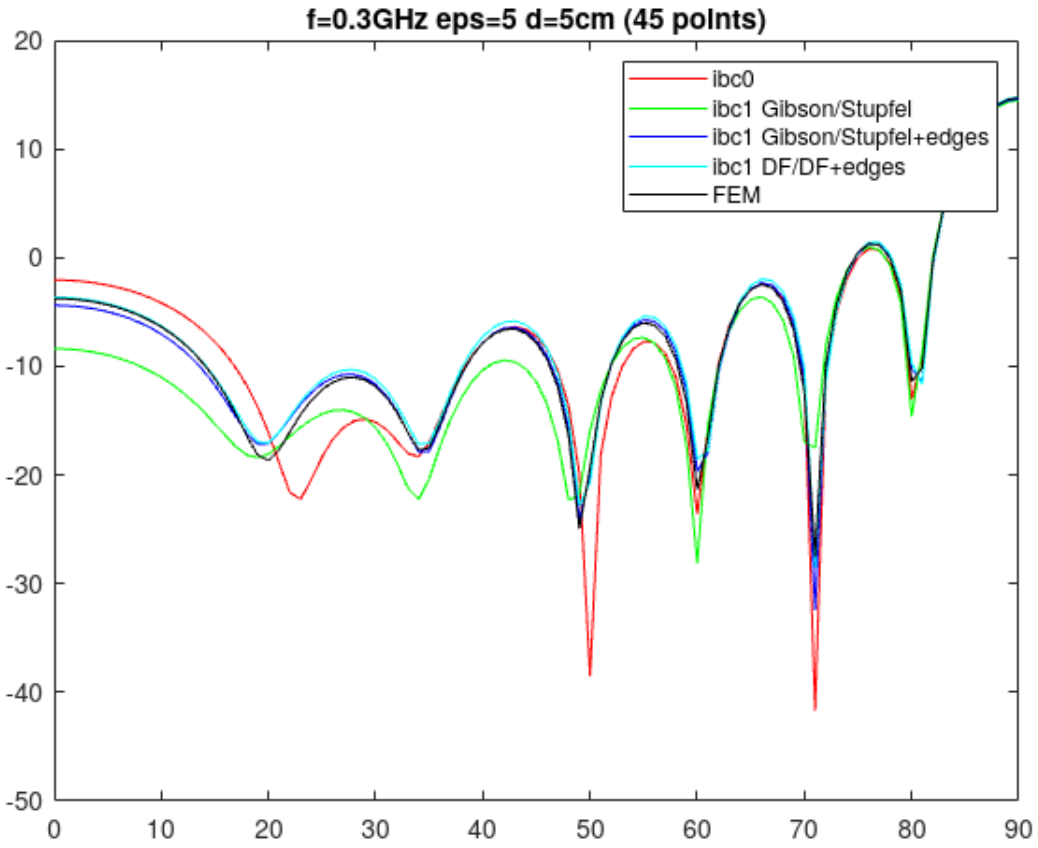

Figure 14: LER d'une rainure rectangulaire de 3m de longueur remplie d'une couche de diélectrique de 0.05m d'épaisseur avec $\epsilon_r = 5.0$, $\mu_r = 1.0$, pour $f = 3.10^8$ Hertz

8 Conclusion

In a first part of this paper, we present an integral formulation with HOIBC to solve Mawwell's equations and validate the method with several numerical results. Then, we apply HOIBC for a ground plane in 2D. We apply Meixner's conditions to take account the ground plane. Now we study discontinuity in 3D.

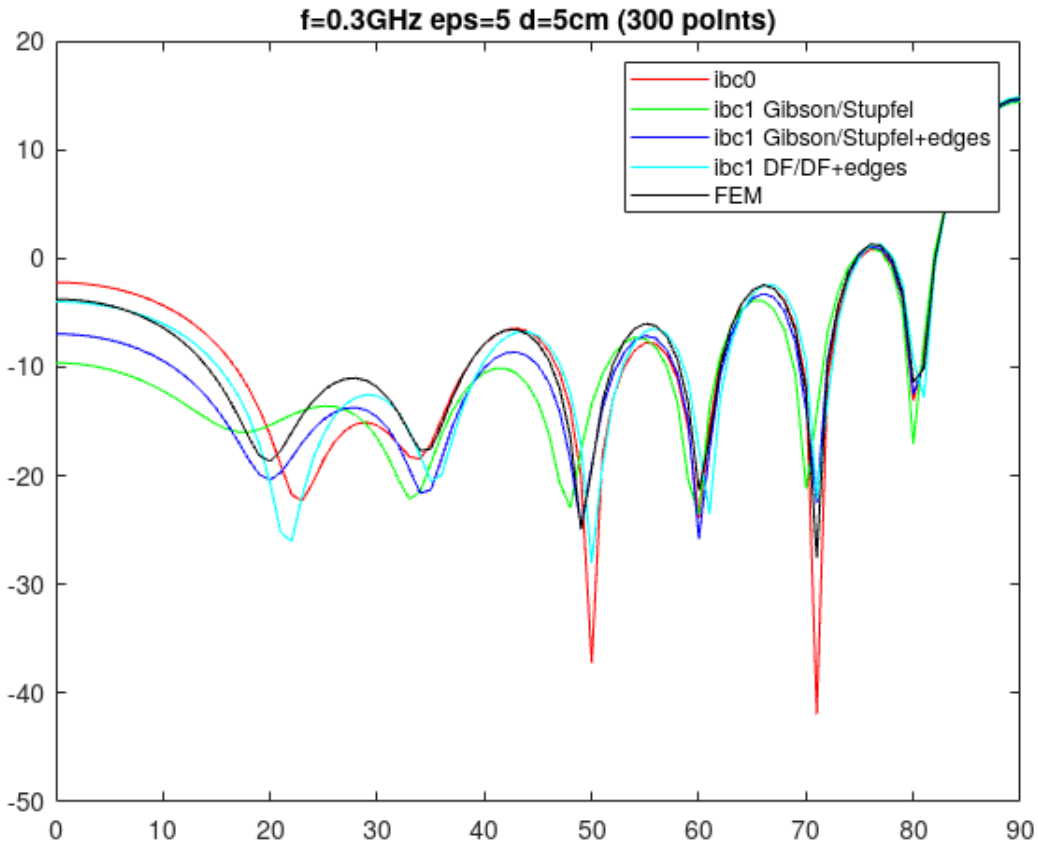

Figure 15: LER d'une rainure rectangulaire de 3m de longueur remplie d'une couche de diélectrique de 0.05m d'épaisseur avec $\epsilon_r = 5.0$, $\mu_r = 1.0$, pour $f = 3.10^8$ Hertz

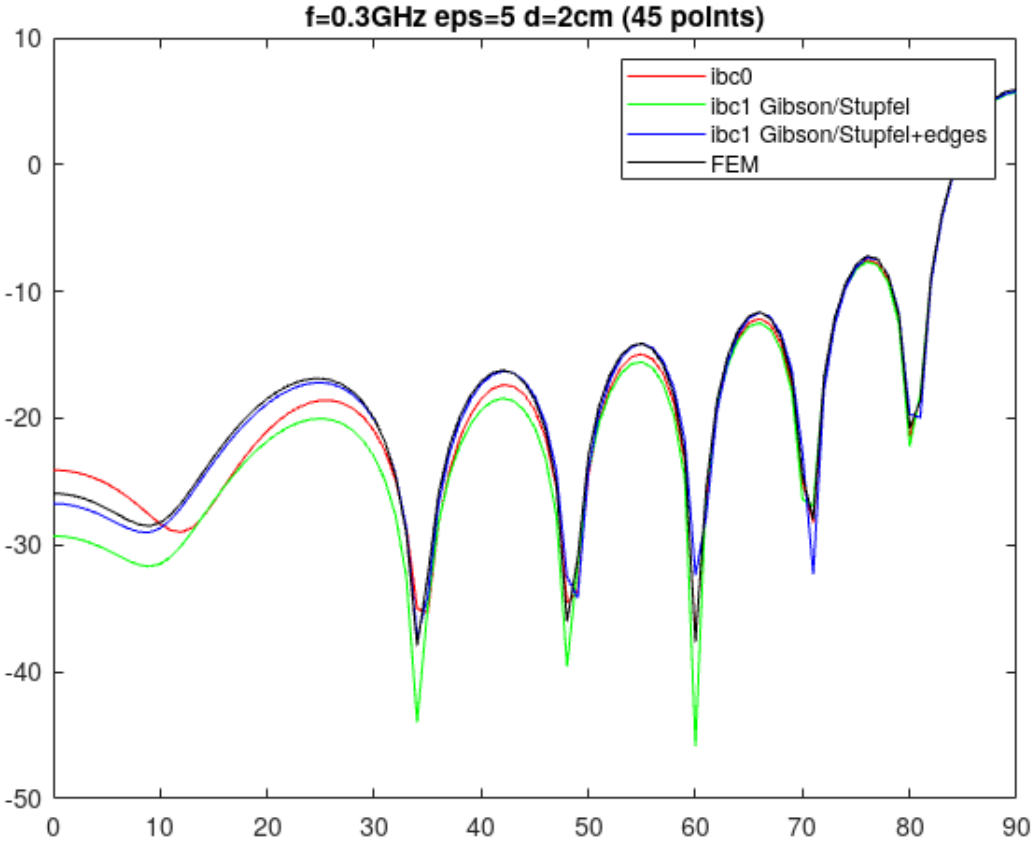

Figure 16: LER d'une rainure rectangulaire de 3m de longueur remplie d'une couche de diélectrique de 0.02m d'épaisseur avec $\epsilon_r = 5.0$, $\mu_r = 1.0$, pour $f = 3.10^8$ Hertz

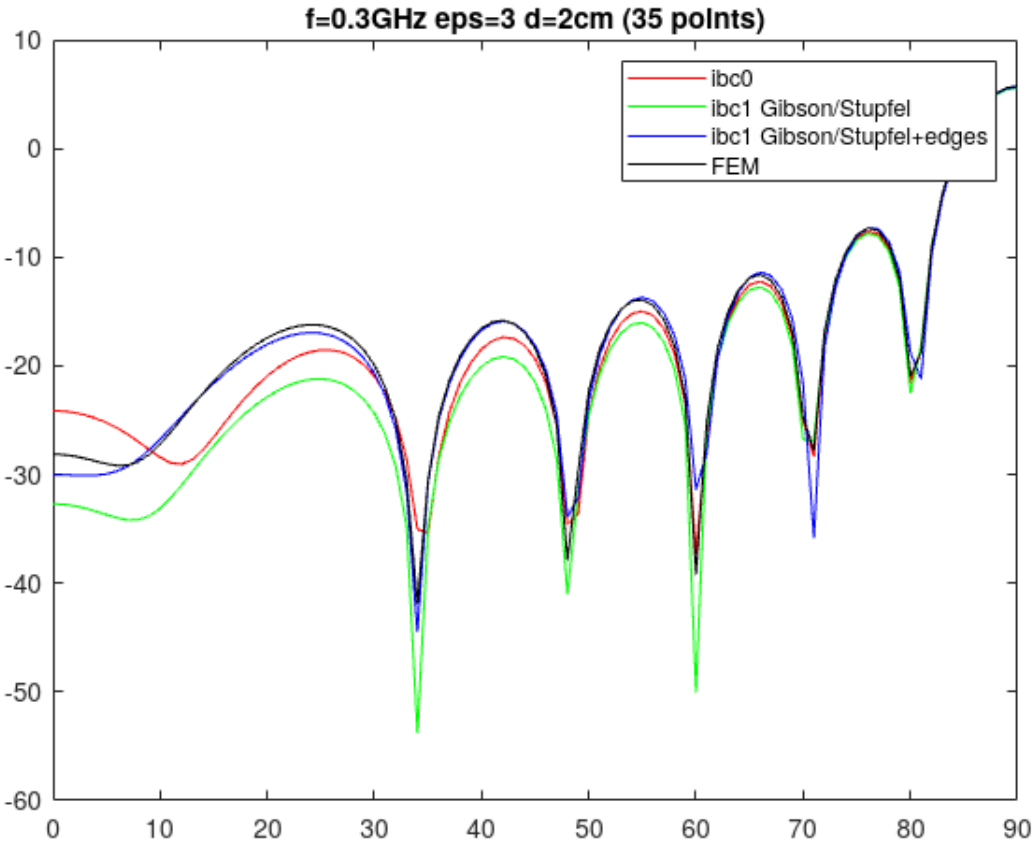

Figure 17: LER d'une rainure rectangulaire de 3m de longueur remplie d'une couche de diélectrique de 0.02m d'épaisseur avec $\epsilon_r = 3.0$, $\mu_r = 1.0$, pour $f = 3.10^8$ Hertz

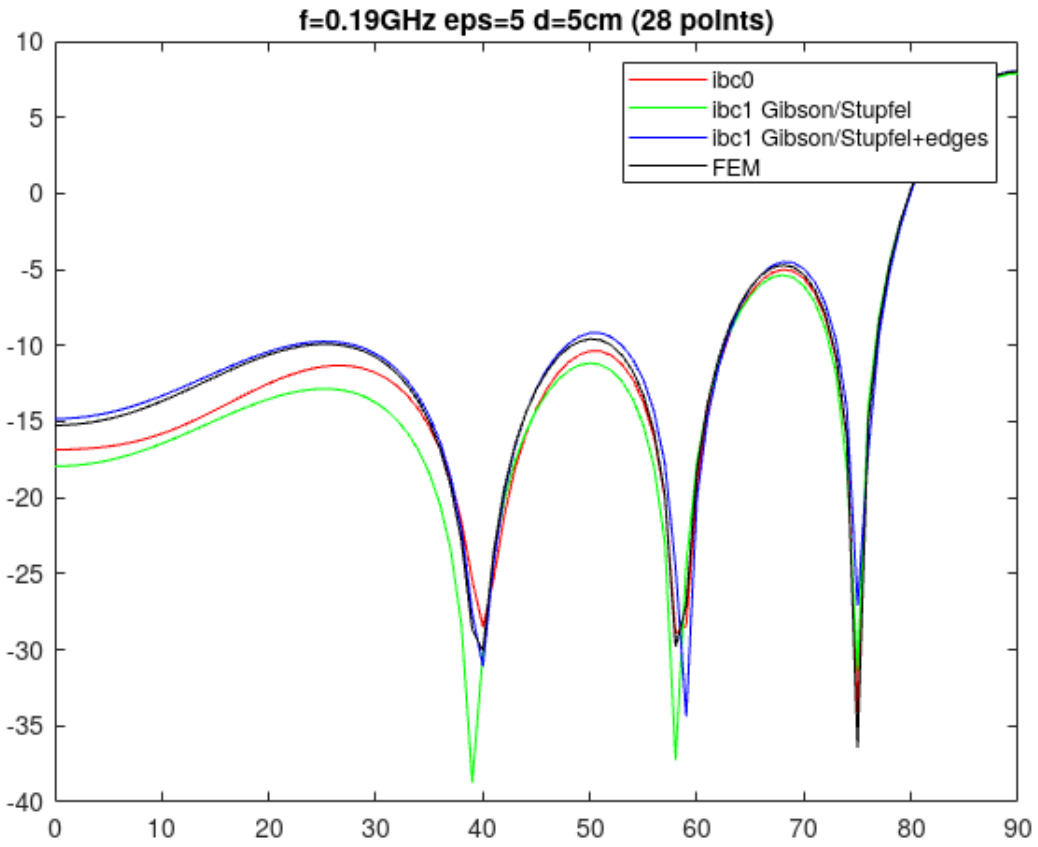

Figure 18: LER d'une rainure rectangulaire de 3m de longueur remplie d'une couche de diélectrique de 0.05m d'épaisseur avec $\epsilon_r = 5.0$, $\mu_r = 1.0$, pour $f = 19.10^8$ Hertz

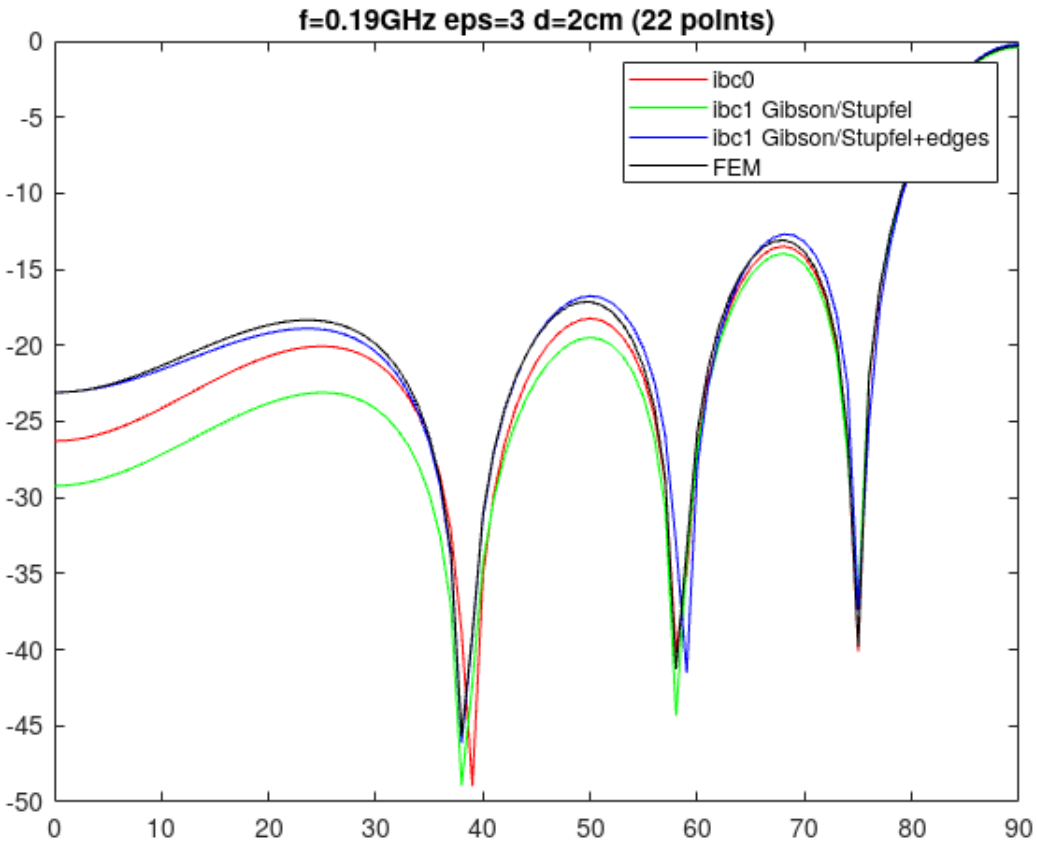

Figure 19: LER d'une rainure rectangulaire de 3m de longueur remplie d'une couche de diélectrique de 0.02m d'épaisseur avec $\epsilon_r = 3.0$, $\mu_r = 1.0$, pour $f = 1,9.10^8$ Hertz

References

[1] A. Aubakirov. *Electromagnetic Scattering Problem with Higher Order Impedance Boundary Conditions and Integral Methods.* Thèse de doctorat, Université Cergy Pontoise, 2014.

[2] Roger F. Harrington. *Time-Harmonic Electromagnetic Fields.* Wiley, 2001.

[3] S. Oueslati. *A new variational formulation for electromagnetic scattering problem using integral method with high order impedance boundary condition - Small perturbations of an interface for Stokes system.* PhD thesis, CY Paris Université, 2019.

[4] M. Kacem. *Méthode intégrale avec une condition d'impédance d'ordre élevé pour résoudre le problème de Maxwell en régime harmonique.* PhD thesis, CY Cergy Paris Université, 2022.

[5] C. Daveau, M. Kacem, S. Oueslati, and S. Bornhofen. Higher order impedance boundary condition with integral method for the scattering problem in electromagnetism. *International Conference on PhotonIcs and Electromagnetics Research Symposium (PIERS)*, 2021.

[6] L. N. Medgyesi-Mitschang P. L. Huddleston and J. M. Putnam. Combined field integral equation formulation for scattering by dielectrically coated conducting bodies. *IEEE Transactions on Antennas and Propagation*, 1986.

[7] M. Taskinen Ylä-Oijala and S. Järvenpää. Surface integral equation formulations for solving electromagnetic scattering problems with iterative methods. *Radio science*, 2005.

[8] J. Jin S. Yan and Z. Nie. A comparative study of calderón preconditioners for PMCHWT equations. *IEEE Transactions on Antennas and Propagation*, 2010.